Sodium storage mechanism investigations through structural changes in hard carbons

Hande Alptekin[1], Heather Au[1], Anders CS Jensen[1,2], Emilia Olsson[1,2,3], Mustafa Goktas[4], Thomas F. Headen[5], Phillip Adelhelm[4], Qiong Cai[3], Alan J Drew[2], Maria-Magdalena Titirici[1*]

[1] *Department of Chemical Engineering, Imperial College London, London SW7 2AZ, UK*

[2] *School of Physics and Astronomy and Materials Science and Materials Research Institute, Queen Mary University of London, London E1 4NS, UK*

[3] *Department of Chemical and Process Engineering, University of Surrey, Guildford, GU2 7XH, United Kingdom*

[4] *Humboldt-University Berlin, Department of Chemistry, Brook-Taylor-Str. 2, D-12489 Berlin, Germany*

[5] *ISIS Pulsed Neutron and Muon Source, Rutherford Appleton Laboratory, STFC, Didcot OX11 0QX, U.K.*

**Corresponding author.*

ABSTRACT

Hard carbons, due to their relatively low cost and good electrochemical performance, are considered the most promising anode materials for Na-ion batteries. Despite the many reported structures of hard carbon, the practical use of hard carbon anodes is largely limited by low initial Coulombic efficiency (ICE) and the sodium storage mechanism still remains elusive. A better understanding of the sodium ion behaviour and possible causes of irreversible capacity in hard carbon anodes is crucial to develop more efficient sodium ion batteries. Here, a series of hard carbon materials with tailored morphology and surface functionality was synthesized via hydrothermal carbonisation and subsequent pyrolysis from 1000 to 1900 °C. Electrochemical results revealed different sodiation-desodiation trends in the galvanostatic potential profiles and varying ICE, and were compared with theoretical studies to understand the effect of the varying hard carbon structure on irreversible capacity and the sodium storage process at different voltages. Furthermore, electrode expansion during cycling was investigated by *in-situ* dilatometry; to the best of our knowledge, this is the first time the technique has been applied to hard carbons in Na-ion batteries. The results showed that the residual or irreversible expansion after one discharge-charge cycle was facilitated the removal of Na-ions from the electrode after desodiation, resulting in an increased ICE after the first cycle. Combining experimental and theoretical results, we propose a model for sodium storage in our hard carbons that consists of Na-ion storage at defect sites and by intercalation in the high voltage

slope region and via pore-filling in the low voltage plateau region; these findings are important for the design of future NIB electrode materials with high capacity and efficiency.

1. INTRODUCTION

The growth in population and improved standard of living have resulted in an increased global energy consumption and is projected to account for an increase in energy demand of 90% by 2035. In light of this, the need to transform the way we produce energy has become a "must do now" operation.[1–3] Renewable energy technologies such as solar, wind, and hydroelectric energy are considered to be the most sustainable energy sources, yet they are intermittent and the peak electrical production will not always match peak demand. Given the increased demand for cheap and efficient large-scale energy storage systems, the need to find an alternative to lithium-ion batteries (LIBs) is becoming urgent. Sodium-ion batteries (NIBs) have received significant attention as a potential eco-friendly and lower cost alternative to LIBs, owing to the abundance of sodium.[1,4] Furthermore, cost benefits may also be achieved by the replacement of expensive copper foils, used as the current collector for LIB anodes, with inexpensive aluminium and by replacing Li salts with Na salts in the electrolyte.[5,6] Additionally, the conceptual similarity make NIBs an attractive alternative to LIBs.[7–12] Nevertheless, both technologies also show considerable differences that need to be overcome before NIBs can be a viable commercial alternative or complement to LIBs.

One of the main limiting factors in transferring the LIB technology to NIBs is that graphite the common LIB anode cannot be applied as an anode material for NIBs.[13,14] The limitation of graphite as a NIB anode material has hence led to alternative anode materials for NIBs being pursued.[15,16] Recently, owing to its high sodium storage capacity, low working voltage, and excellent cycling stability, hard carbons with randomly oriented, disordered graphitic layers with "closed" micropores formed between these domains have been intensively studied as a NIB anode material, with promising performance being reported.[17–19] These anodes can be derived from cheap and sustainable bio-sources, a key factor promoting its commercialisation for low cost and sustainable energy storage.[17,20–28] However, there is still a major barrier to realizing large-scale application of hard carbon: capacity loss after first cycle which results in low initial coulombic efficiency (ICE). Earlier researches often associate the low ICE with undesirable the parasitic reactions causing to solid electrolyte interphase (SEI) formation on hard carbon surface.[29–31]However, no direct relationship was founded between specific surface

area of hard carbons (Brunauer, Emmett and Teller (BET) specific surface area) and the ICE. Some studies have reported that the ICE cannot be increased significantly even in hard carbon with very small specific surface area materials. For example, Ji et al.[32] reported that sucrose-derived hard carbon pyrolyzed at 1100 °C for 6 h, has a low surface area (5.4 m2 g−1) with 78% ICE and Cao et al. reported hollow carbon nanowires[29] and hollow carbon nanoparticles[33] pyrolyzed at 1150 °C and the specific surface area is 34.1 $m^2 g^{-1}$ and 23.5 $m^2 g^{-1}$, respectively. Although the surface area of the first is 30% smaller than the that of the second, ICE only shows 1.2% improvement from 50.5% to 51.6%.

This shows that there are different factors that play an important role on higher initial coulombic efficiency for example, obtaining optimum morphology with certain ordering, number of defects and pores, while ensuring an optimum flexibility and mechanical stability of electrode during cycling. The effect of pyrolysis temperature on the structural evolution and electrochemical performance of the hard carbon has been extensively investigated.[34–37]As a common trend, simultaneous decrease in surface area and the number of defects in hard carbon, and an increased degree of graphitization were observed with an increase in heat treatment temperature. All these morphological differences also create different electrode architecture and dynamics which have considerable influence on the electrode's stretching and strain during the battery cycling. In order to investigate the dynamic behaviour of the batteries, several *in situ* techniques have already been applied successfully, either on the cell, electrode or material level during the electrochemical cycling. One possible technique that allows indirectly to reveal the dynamic behaviour of crystalline anodes at the atomic level is *in-situ* X-ray diffraction (XRD).[38–40] Also, *in-situ* Atomic Force Microscopy (AFM) can be used to study the volume change of active electrode particles during the electrochemical cycle.[41–43] The most suitable method to investigate the dynamic changes of electrodes during electrochemical cycle is *in-situ* electrochemical dilatometry (ECD).[44–49]

The Na-ion storage mechanism is one of the other important factors that have an effect on the ICE of the hard carbon anode.[50] Despite reports of numerous promising hard carbon materials, discrepancies in the understanding of sodium storage mechanism are still exist. [51,52] In the characteristic charge-discharge potential profiles two distinct voltage region have been observed; a sloping region above 0.1 V, and a plateau below 0.1 V. In earlier studies, these two distinct regions are assigned to different sodium storage mechanisms. The first model reported by Stevens and Dahn[53] and assigned the sloping region to sodium ion insertion between graphene layers, and the plateau region to sodium filling or plating into pores. Later, Komaba

et al.[54] supported this mechanism by using *ex-situ* XRD, hard carbons was discharged to 0.1 V, and expanded interlayer spacing was observed because of sodium ion insertion. *Ex-situ* small angle X-ray scattering (SAXS) analysis of the sample that discharged below 0.2 V showed a decrease in the intensity in pores, indicating that sodium ions inserted into the nanopores within this voltage range. Tarascon et al. tuned the microstructure of PAN derived CNF under various carbonization temperatures. By using X-ray photoelectron spectroscopy (XPS), temperature-programmed desorption coupled with mass spectrometry (TDP-MS) and gas adsorption techniques, the slope region between was attributed to sodium ion adsorption on disordered graphene sheets and the plateau region to the sodium ion filling into pores. The different mechanisms found in the literature may result from comparing carbon materials from different origins. Besides the type of materials, the applied experimental conditions and the characterization techniques used, and differences in detailed chemistry, especially heteroatomic doping, may be the cause of different conclusions.

In this paper, we synthesised hard carbon series derived from hydrothermal treatment of glucose with citric acid as a catalyst (GCs) which were further carbonized at different temperatures. The resulting hard carbons exhibited a variety of textures and structures, all furthermore showing different electrode architectures with different degrees of surface functionality and defects, varying number and size of pores and distinct electrochemical behaviour and coulombic efficiencies. With the support of experimental and theoretical studies, modified structures were used to investigate the effect of hard carbon structure on ice and the sodium storage mechanism. A fundamental understanding of the hard carbon morphology, the influence of discrete morphologies on the electrode dynamics during sodium insertion and removal and the sodium storage mechanisms is essential for efficiently designed hard carbon materials for high capacity and high efficiency NIBs.

2. RESULTS AND DISCUSSION

The SEM micrographs (Figure S1) show that the GCs have a spherical shape with a relatively narrow particle size distribution, ranging from 5 to 8 μm. No change in particle size was observed upon pyrolysis, suggesting that the particle size is primarily determined by the Hydrothermal Carbonization (HTC) process which takes place at low temperatures.[55] The coating process for electrode preparation did not change the GCs` material morphology and no changed were observed in the particle size (Figure S1f). Small angle neutron scattering (SANS) and small angle X-ray scattering (SAXS)[56] were used to determine pore sizes. The pore size

was modelled using a Guinier-Porod equation.[56] SANS (Figure 1a) and SAXS (Figure S2) data shows Guinier plateau at around 0.1 $Å^{-1}$ indicating dilute nanopores of random size and shape (Figure S2g). From this, the average pore size was determined (Figure 1c) and showed a small increase from 1.5 to 2 nm between 1000 ºC to 1500 ºC, followed by a sharper increase to 3.3 nm at 1900 ºC (Figure 1c). The pore size was also characterized by N_2 and CO_2 gas adsorption (Figure S4). The N_2 adsorption showed low surface area below 11 m^2/g for all samples (Table 1), suggesting that there is little to no open porosity. Due to the higher saturation pressure and smaller size of molecule, CO_2 is more efficient at penetrating into the material[57] and showed a much higher surface area of 496 m^2/g and a pore size of 0.5-0.8 nm for all samples, significantly smaller than pore sizes compared to the SAXS/SANS analysis. The CO_2 adsorption surface area furthermore decreases with increasing temperature to just 2.6 m^2/g for the high-temperature sample. In SAXS, change in surface area can be analysed by the Guinier-Porod region[56] (Figure S2h) which is proportional to the surface area of the nanopores. SAXS/SANS measurements show a minor decrease in the surface by increasing carbonization temperature as compared to gas adsorption measurements. This suggests that, with increasing carbonization temperature, closed pores can be formed that are not accessible for gas probing but can be measured by X-ray and neutron scattering.

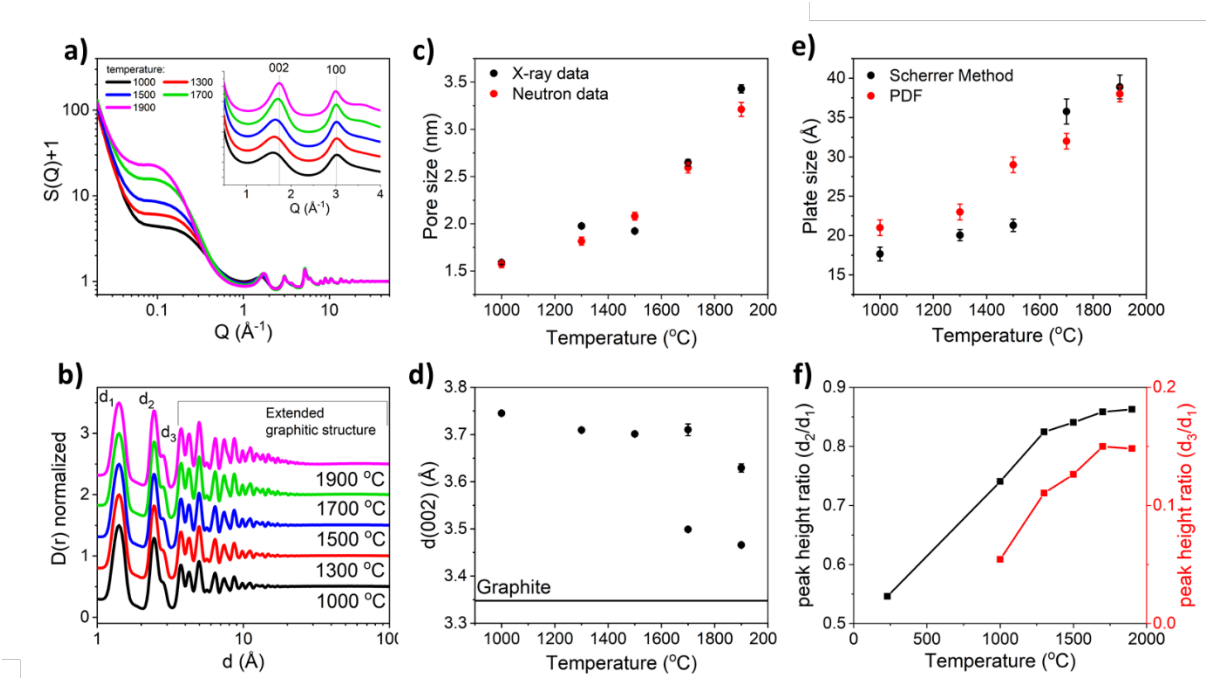

Figure 1. a) Structure factor (The Guinier-Porod region showing scattering of the nanopores (Q<1 Å-1) and scattering from the atomic structure at higher Q) and b) pair distribution functions (PDF)of the

GCs with the PDF normalized to the height of the first peak at 1.5 Å c) Mean pore size determined from the Guinier-Porod region of the SANS and SAXS data d) Interlayer spacing of the graphitic planes e) size of the basal plane determined using the Scherrer method and the PDF, and f) peak height ratio of the first three peak observed in the PDF (Figure 1b)

A graphitic local structure with turbostratic stacking of the basal plane is observed in the neutron total scattering (Figure 1a) and WAXS measurements (Figure S2). The data show the characteristic peaks from the plane of the (002) and (100) reflection at 1.8 and 3 $Å^{-1}$, respectively. The interlayer distances (d_{002}) (Figure 1d) showed that the average interlayer distance is ~3.75 Å below 1500 ºC, well above the limit where sodium intercalation in graphitic layers is energetically favourable. (cite Emilia's paper on intercalation energies or the muon paper which also contains this result). At higher temperatures the 002 peak shifts to shorter distances and the peak shape becomes asymmetrical, requiring a two peak model to achieve a decent fit (Figure S2e), this suggest that as the graphitic domains develop some domains are not able to grow along the *c-axis* likely due to steric constraint. Therefore, a formation of two distinct populations in interlayer distance (Figure 1d) are observed in the higher temperature materials. The mean size of the graphene domains was determined by the Scherrer equation using the width of peak from the plane of the (100) reflection (Figure 1a) and directly from the pair distribution functions (PDF) (Figure 1b). Both techniques showed an increased domain size from ~2 nm at 1000 ºC to ~4 nm at 1900 ºC (Figure 1e), which is an indication of structural ordering. The increase in the graphene domain size is associated with a simultaneous increase in the pore size, suggesting that the pores dimensions are determined by the size of the graphene domains. The TEM images (Figure 2) show that all samples have typically disordered carbon structures, although more organised regions with longer graphitic domains appear with increasing the carbonisation temperature. Due to the presence of strong crosslinks formed during HTC, even at 1900°C, material still shows the characteristics of hard carbon as the temperature was not sufficient to transform the structure to a highly ordered graphitic morphology. This is corroborated by a sharpening of the D- and G-bands and an increase in the I_D/I_G ratio (Table 1) observed from Raman spectroscopy (Figure 2f), suggesting more order at higher treatment temperatures. For non-graphitic carbons, a higher I_D/I_G indicates the presence of a greater number of aromatic 6-membered rings, and therefore a higher degree of graphitic order.[58,59] However, the presence of a large D-band for the sample treated at 1900 ºC suggests that many defects are still present in the most ordered sample.[60] The appearance of the 2D peak at 1700 and 1900°C implies the presence of larger domains of graphitic ordering,

consistent with the neutron total scattering and SAXS/WAXS results and observations made by TEM .[58–61]

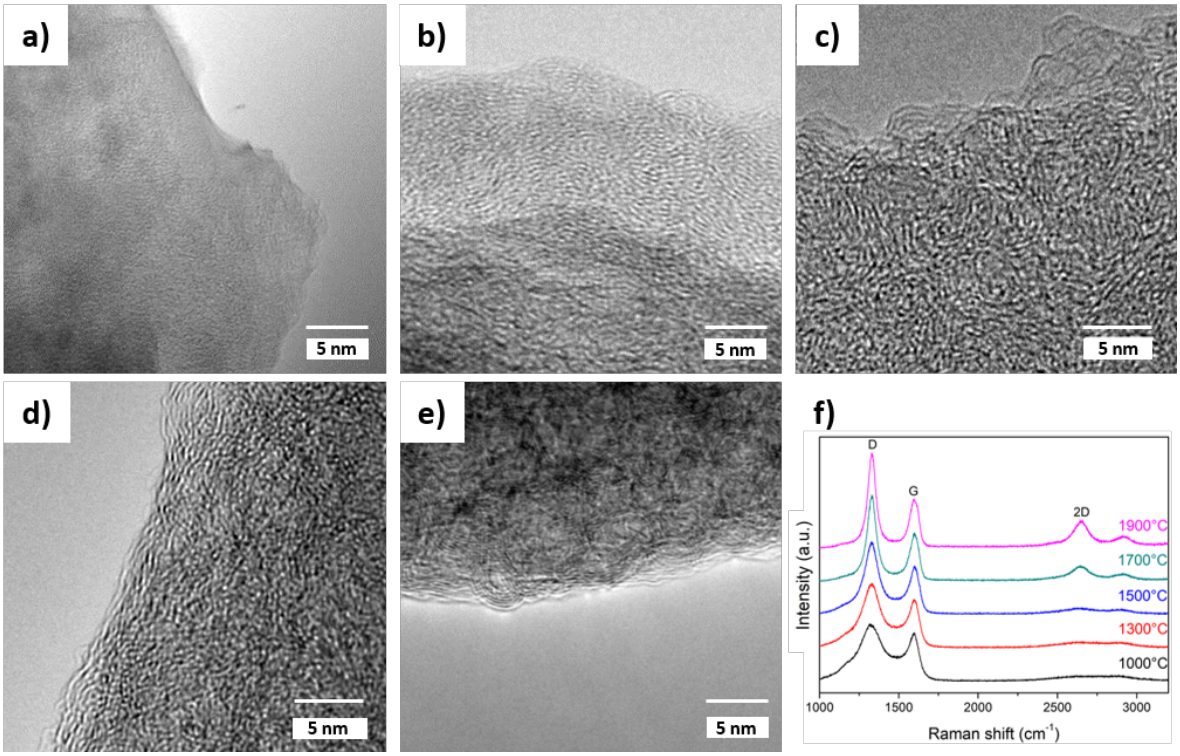

Figure 2. TEM images of a) GC1000, b) GC1300, c) GC1500, d) GC1700, e) GC1900, and f) Raman spectra as a function of carbonization temperature.

The PDF can be used to observe changes in the local structure (Figure 1b). The peak at ~1.3 Å (marked as d_1) corresponds to the direct C-C and C-O bonds (a schematic of all the relevant distances is provided in Figure S3 in the supporting information). The peak at ~2.8 Å (marked as d_2) relates to the second nearest neighbouring carbon and the presence of the signal at ~3.1Å (marked as d_3) indicates that the structure has the characteristic interatomic distance of the C1-C4 distance in a 6-membered aromatic ring structure. An increase in the ratio of the d_2/d_1 peak (Figure 1f) shows that increasing carbonization temperature causes higher average number of carbons in the 2nd nearest neighbour position compared to the number of directly bonded carbons. The difference between the ratio of the d_2/d_1 is largest between the precursor (HTC sample before pyrolysis) and GC1000, as expected given that the HTC sample is dominated by 5-membered ring structures, aliphatic chains and contains few aromatic compounds.[62] The difference between the d_2/d_1 ratios is also relatively large between GC1000 and GC1300. This difference decrease after GC1300, which shows that there is still reactive parts left up to 1300 °C, likely linked to defects and crosslinkers between the graphitic domains that can act as

feedstock for the formation of new graphitic domains as the size of the graphitic domains to not change much in this temperature range. Above 1500 ºC the changes are likely related to removal of edge terminations as the basal plane increases from 2 to 4 nm (Figure 1d and 1e). This is supported by the increase in the d_3/d_1 intensity ratio, suggesting a higher density of aromatic structure with increasing carbonisation temperature. The presence of heteroatoms in the GCs was also investigated by X-ray photoelectron spectroscopy (XPS) to evaluate the Faradaic reactions which may occur on the surface of the electrode material.[63,64]The XPS analysis (Table 1) indicates that there is an increase in carbon content (C1s, %) and a decrease in oxygen content (O1s, %) with increasing carbonization temperature. The amount of defects and functional groups are changing in the same way with the carbonization temperature.[65]Overall the high-temperature materials have fewer functional groups and defects, narrower interlayer distances and larger pore sizes compared to the low-temperature materials.

Table 1. Summary of the characteristics of the GC materials. SN2 and SCO2 surface area determined by N2 and adsorption CO2 adsorption respectively. C1s and O1s are atomic compositions obtained by XPS.

Materials	GC1000	GC1300	GC1500	GC1700	GC1900
d_{002} (Å)	3.75	3.68	3.66	3.58	3.43
d_{100} (Å)	2.04	2.04	2.04	2.05	2.10
Pore Size $_{SAXS}$ (nm)	1.6	2	2	2.6	3.5
I_D/I_G	1.15	1.32	1.50	1.82	2.02
S_{N2} (m^2g^{-1})	11	4	2	1	0.5
Pore Size $_{N2}$ (nm)	1.6	2.7	2.8	2.9	4.8
S_{CO2} (m^2g^{-1})	496	164	76	5.2	2.6
C1s, %	86.2	89.6	90.3	97.6	97.8
O1s, %	13.8	10.4	9.7	2.4	2.2
1st Cycle Capacity (mAh g^{-1})	265	301	210	81	66
Initial Coulombic efficiency %	72	83	74	76	66

To observe the effects of all these structural differences on the electrochemical storage performance, GCs were electrochemically tested in half-cell configuration with Na metal as the counter electrode. Figure S5 shows the first three cyclic voltammogram (CV) curves of the GCs at a scan rate of 0.1 mVs^{-1}. In the first cathodic scan of all the samples, the broad peak at around 0.4 V may be attributed to the reactions of the active sites on the carbon anode material with solvent molecules and electrolyte ions leading to the formation of the solid electrolyte interphase (SEI) in the first cycle.[28] The irreversible area under the broad peak of GC1000 is much higher compared to the higher temperature materials, due to the higher number of defects

and surface functional groups present which react irreversibly with the electrolyte. Additionally, GC1000 has a larger specific surface area which facilitates SEI formation, and also contributes to the initial irreversible capacity. A sharp peak in the low potential region of 0.1 V can be ascribed to the Faradaic reduction reactions such as oxidation, reduction reactions that involves electron transfer.

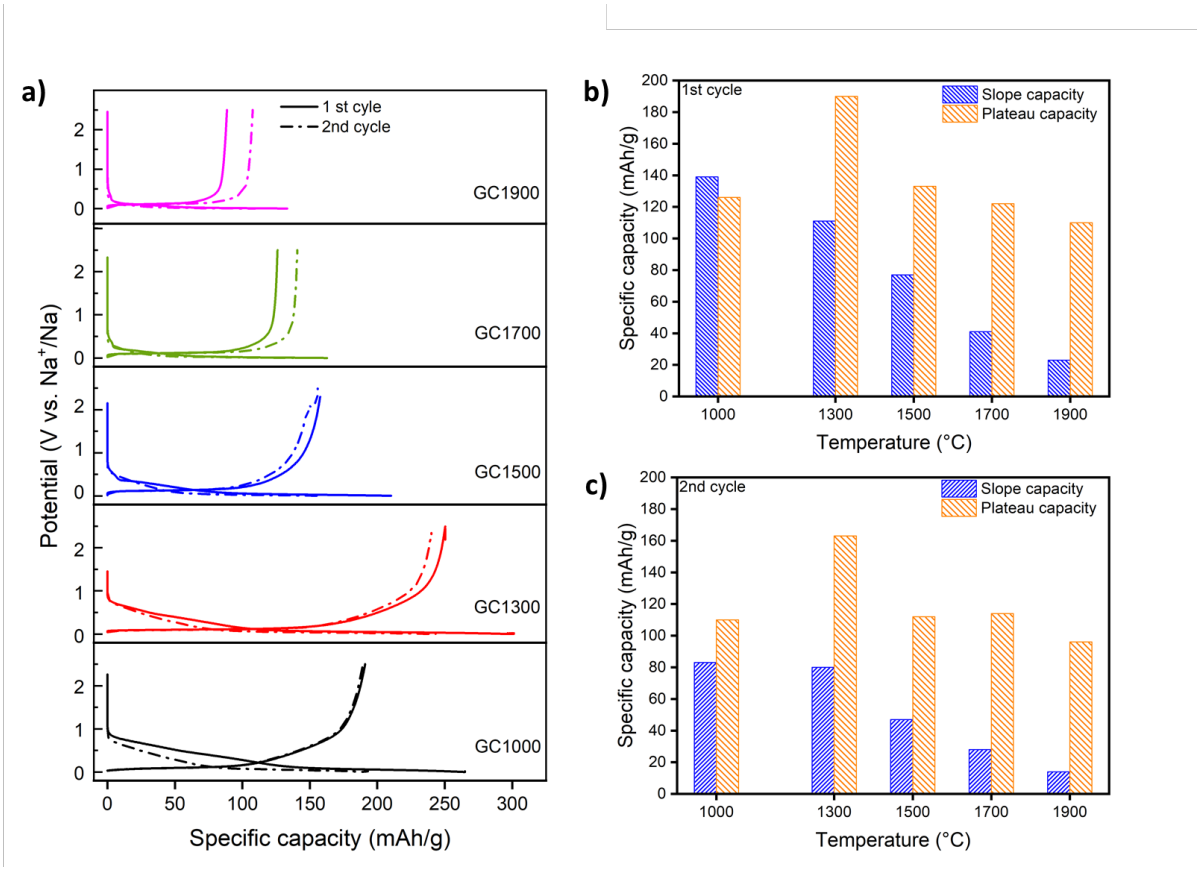

Figure 3. a) The galvanostatic sodiation (discharge) and desodiation (charge) potential profiles of GC1000, GC1300, GC1500, GC1700 and GC1900. High voltage sloping region and low voltage plateau region capacities b) in the first cycle and c) in the second cycle.

Figure 3a shows the galvanostatic potential profiles of the first and second discharge-charge cycles for the hard carbons tested at 0.1 C. GC1300 delivers the highest total discharge capacity of 301 $mAhg^{-1}$ with an ICE of 83% (Table 1). The voltage profile can be divided in to two regions, the high voltage sloping region between 1 and 0.1 V and the low voltage plateau region around 0.1 V. These separate regions' capacities were evaluated from the discharge profiles in the first (Figure 3b) and second cycle (Figure 3c). As the carbonization temperature increases, the sloping region capacity contribution decreases in both the first and second cycles. GC1000 with the highest oxygen content shows the largest capacity contribution in the sloping region (Figure 3b and 3c), consistent with previously proposed sodium storage models where oxygen-

containing defects offer favorable sodium adsorption sites.[66,67] Besides the contribution of surface functional groups and defects, variations of interlayer distance (d_{002}) between graphitic layers also affect Na insertion, as the expanded graphitic layers serve as Na storage sites. Therefore, a larger contribution to the sloping region is seen in the lower temperature hard carbons with larger interlayer distance as compared to the higher carbonization temperatures. Whilst the material carbonization temperature increases, more than 60% of the total capacity is gained from the low plateau region in both the first and second cycle. The enhanced plateau capacity in high temperature materials might be attributed to an increasing number of wider pores created with increasing carbonization temperatures, providing additional Na storage sites.

An optimum concentration of internal (closed) microporosity is important to maximize the storage capacity. However, the open pores which cause the large external surface area should be kept low to prevent SEI formation and resulting irreversible capacity. As previously mentioned, the N_2 adsorption showed very low surface area for all samples (Table 1), suggesting that there is little to no open porosity in any of the materials, yet there is still irreversible capacity observed. Therefore, this shows that there are other parameters rather than just surface area that cause low ICE. To understand such other factors causing low ICE along with the effects of morphological changes on electrochemical performance, a more detailed study was conducted using *in-situ* electrochemical dilatometry (ECD) (Figure S6a). From these measurements, the maximum expansion and breathing ability (irreversible expansion, defined in Figure S6b) of the different electrode morphologies were observed over the first three sodiation-desodiation cycles. The initial thicknesses of GC1000, GC1300, GC1500, GC1700, GC1900 (film thickness without Al foil) were 104 µm, 162 µm, 127 µm, 94 µm, 81 µm and the first sodiation of the hard carbons leads to an increase in electrode thickness by about ~2.2 %, 2.6 %, 2.3 %, 2.3 %, 0.7 %, respectively. The hard carbon expansion is very small compared to that of graphite (200%)[68] confirming the structural stability of hard carbon electrodes. The thickness changes obtained in the first sodiation are different in the following sodiation cycles. After the first cycle was completed, permanent structural changes were observed in the electrode thickness compared to the initial state. GC1300 (Figure 4) has the highest percentage (1.03 %) of breathing at the end of the first cycle, and also the highest ICE (83%) among them, while GC1900 shows the lowest breathing percentage (0.25%) and lowest ICE (66%). Based on these results, a correlation between electrode breathing ability after first cycle and ICE was

identified; the residual expansion in the electrode facilitates easier removal of Na-ions from the structure during desodiation resulting in an increased ICE.

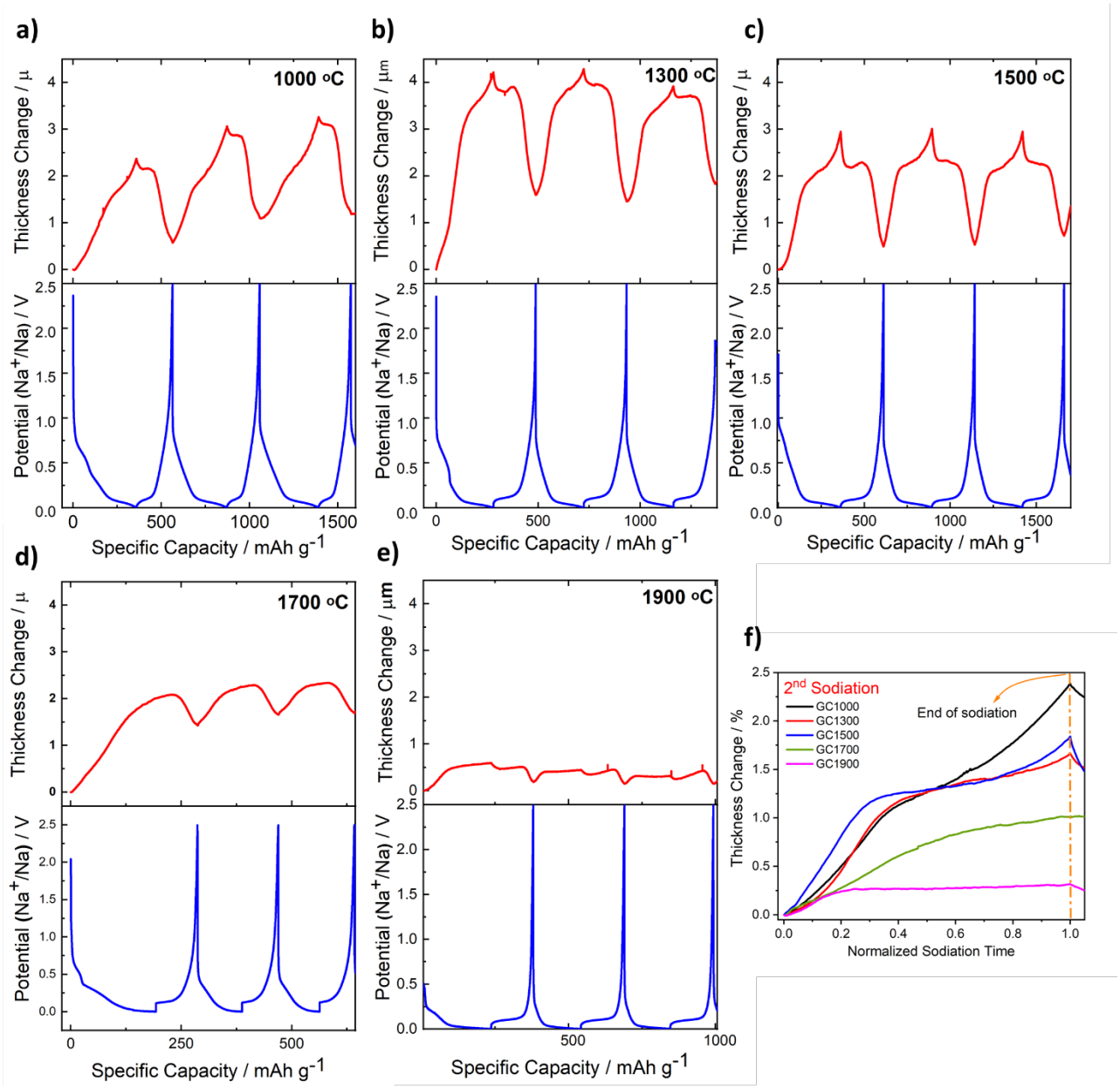

Figure 5. a) In-situ electrochemical dilatometry measurements of electrode thickness change in the first three cycles for a) GC1000 b) GC1300 c) GC1500 d) GC1700 and e) GC1900 f) percentage thickness change of each electrodes during the second sodiation.

The e*x-situ* SEM images of GC1300 (Figure S7) show cross-sections of the electrode after the first sodiation and desodiation process. Because the electrode has a variable surface height, three different regions were measured to obtain the average (average thickness before cycling ~144, after first sodiation ~178 µm, after first cycle ~170 µm) and the result is consistent with

the *in-situ* electrochemical dilatometry observation that the structure remained expanded as compared to the initial state of the electrode.

In relation to the storage mechanism, *in-situ* electrochemical dilatometry results generally show a larger increase in thickness during the sloping region than in the plateau region, implying that a sodium storage process associated with a large volume change is occurring at these voltages. To reduce the effect of the electrode dynamics variation observed in the first cycle, the second cycle was taken into consideration in observing the ion storage mechanism. Moreover, the percentage thickness change of the electrodes (Figure 4f) in the higher temperature samples is much smaller than in the low temperature samples, although still observable. This trend in thickness change can be correlated with the decreasing interlayer spacing with increasing temperature; at low temperatures, the many domains with wider interlayer spacing allow easy Na-ion intercalation, and the structure expands to accommodate insertion, resulting in a large thickness change. In the higher temperature materials, fewer of these expanded domains are available for sodium intercalation, therefore a smaller electrode expansion is observed. During the plateau region, a much smaller thickness change is observed at higher temperatures for the GC1700 or GC1900 samples (Figure 4f) which can be explained by a pore filling mechanism in this voltage region. Larger pore sizes in the higher temperature materials (Table 1) can compensate the thickness change of the whole electrode during ion insertion.

From the experimental characterisation of the hard carbon samples above, it was shown that the materials contain expanded graphitic stacks with different interlayer distances and graphitic surfaces with oxygen heteroatom defects. To bring atomistic insight into the effect of oxygen-containing surface defects and differing graphitic interlayer distances on the sodium storage and incorporation in the hard carbon samples, density functional theory (DFT) simulations were employed. The surface defects and oxygen heteroatoms on the hard carbon surfaces were modelled in terms of oxygen defects on a graphene monolayer, whereas to understand the difference in intercalation behaviour for the different hard carbon samples with varying graphitic interlayer distance, a double layer planar graphitic model was employed. The effect of pore size on sodium incorporation in hard carbon was probed in a previous publication (ref Emilia computational paper). To study the effect of different interlayer spacing on the sodium incorporation and migration, the sodium binding energy in bi-layer graphitic layers with different d_{002} was calculated (see supporting information for details). To calculate the sodium binding energy (E_{bind})[69–71], equation S1 was adapted to include sodium in between two graphitic

sheets, and the energy of the system with two graphitic sheets without sodium. The calculated binding energies are presented in Table S1. Comparing the sodium binding energies in Table S1 (with the more negative E_{bind} indicating a more energetically stable structure), it is clearly seen that the sodium incorporation in the graphitic stacks become more favourable with increasing d_{002}. Hence, GC1000 is the most favourable for sodium intercalation from these calculations, whereas GC1900 would not be expected to store much sodium in the graphitic stacks with average d_{002}. The sloping region is partly attributed to sodium storage in graphitic stacks. Hence, a stronger (more negative) E_{bind} is in line with the more distinct sloping regions observed for the GC1000, GC1300, and GC1500 samples as compared to GC1900. The GC1700 would from the calculated E_{bind} also have contribution from graphitic stack filling in its sloping region but does have a distinctly smaller sloping region than the lower carbonisation temperature samples. Comparing the intercalation energy per sodium atom at different sodium loading in the graphitic models with different interlayer distance (Figure 5), it is clearly seen that sodium intercalation in GC1900 is energetically unfavourable. GC1900 would hence be expected to have a lower sodium intercalation potential than the samples with higher average interlayer distance. The calculated intercalation energies also show that sodium intercalation increases with increasing interlayer distance (Figure S8), which could explain the higher sloping region capacities measured for the GC1000, GC1300 and GC1500 samples compared to high temperature materials.

To assess the effect of oxygen-containing defects on sodium storage, which would contribute to the sloping region, sodium ion selection of graphene defects was modelled were (Figure S8). These defects have not been explicitly shown to be present in the experiments above but will serve as a guide to how oxygen-containing defects influence the sodium adsorption. In a previous publication, the effect of a wider selection of graphene defects on sodium adsorption was investigated, and reference to that study will be made here.[72] For each postulated defect in Figure S8, its equilibrium defect formation energy (E_f^{defect})[73–75] was calculated (see the supporting information). The calculated E_f^{defect} are collected in Table S3 and show that oxygen-containing defects are energetically favourable on the graphene basal plane. Comparing E_f^{defect}, none of the here investigated defects have higher E_f^{defect} than the $3O_C$ defect, or lower than the $2O_C$ defect. The formation energies of the O_C and $2O_CV_C$ defects are furthermore relatively low, which indicates that a high concentration of these defects in the hard carbon basal planes would be probable. This confirms the experimental observation that

hard carbons are prone to the formation of oxygen surface defects. To assess the sodium storage on these defective surfaces, the sodium adsorption energy (E_{ads}^{Na}) [69–71] was calculated (equation S1). The more negative the adsorption energy is, the stronger the adsorption. The calculated adsorption energies for sodium on defect site are collected in Table S2. The presence of oxygen-containing defects improves the sodium storage capacity of the carbon surface, except for the O_C defect (-2.85 eV) which shows no change in the sodium adsorption energy. The strong sodium adsorption energies calculated for the O_CV_C defect indicate that this defect would greatly improve sodium storage. Hence, in the hard carbon samples with more oxygen content and oxygen surface defects, i.e. GC1000, GC1300, and GC1500, a considerable amount of the sodium would be expected to be stored on defect sites. Therefore, a larger contribution to the sloping region capacity due to the presence of these kinds of defects in the lower temperature sample would be expected as compared to the GC1700 and GC1900 samples. This is consistent with XPS results in Table 1, GC1700 and GC1900 have a lower oxygen content than the lower temperature samples, and hence the contribution from sodium storage on defect sites in the GC1700 and GC1900 samples will be much less, with the major sample will be much less, with the major contribution to the GC1700 sloping region coming from the graphitic stack filling. Hence, the sloping region of GC1700 is much shorter than for GC1000-1500.

3. CONCLUSIONS

In this study, a series of hard carbon materials derived from glucose was produced, and the effect of the different hard carbon configuration on coulombic efficiency and the sodium storage mechanism investigated by using TEM, Raman, XPS, SAXS/WAXS, SANS, and gas adsorption techniques. It demonstrates that the presence of oxygen defects and large interlayer spacing has a larger contribution to the sloping region which is also supported by DFT simulations. showing that sodium intercalation ability increases with increasing interlayer distance, whereas oxygen-containing surface defects improves the sloping region capacity. Increasing the number and size of pores with increasing carbonization temperatures enhanced capacity gain from plateau region. This led us to hypothesize that the slope region capacity due to sodium ion adsorption on disordered graphene layers and intercalation into graphene layers with suitable spacing, in the plateau region sodium ion storage mechanism dominates over pore filling. The correlation between initial coulombic efficiency and the dynamic behaviour of the electrode provided by *in-situ* electrochemical dilatometry for the first time and results shows

that the breathing ability of the electrode during cycling, facilitates detachment of the sodium ions from the electrode during desodiation and exhibits higher the Columbic efficiency. These findings will enable the improved design and modification of appropriate electrode structures and chemistries allowing us to move closer to electrochemically optimized, high performance and efficient Na ion batteries.

Experimental Methods

Materials synthesis: Hard carbon material used in this research was prepared from glucose in two steps that consist of hydrothermal carbonization at low temperature and carbonization at high temperature.[55] In the first stage, 10 gr glucose (D-(+)-glucose, ≥99.5%, Sigma Aldrich) was dissolved is 90 ml deionised water and the pH adjusted to 1-2 by the addition 3.6 gr of citric acid (≥99.5%, Sigma Aldrich). The solution was placed in a Teflon container, then inside a stainless-steel autoclave vessel and heated at 230ºC for 12h then dried at 80 ºC overnight. In the second stage, the resulting material was pyrolysed under continuous nitrogen gas flow in a tube furnace for 2 h with a heating rate of 5^{o}C min^{-1}. Pyrolysis was conducted at 1000^{o}C, 1300^{o}C, 1500^{o}C, 1700^{o}C and 1900 ºC (denoted GC1300, GC1500, GC1700, GC1900)**.**

Materials characterization: The morphology and structure of the samples were characterized by FEI INSPECT F Scanning Electron Microscope (SEM). Samples after cycling were washed with dimethyl carbonate and dried at 25 °C under vacuum overnight. For cross section measurements, electrodes were cut by scalpel. Transferring time for air sensitive sodiated samples was 60 s at maximum. A JEOL JEM-2010 Transmission Electron Microscope (TEM). The textural properties of the GCs were determined from the adsorption isotherms of N_2 at 77 K and CO_2 at 273 K using Autosorb iQ-C (Quantachrome Instruments, USA) instrument. The specific surface areas were calculated by Brunauer-Emmett-Teller (BET) method for N_2 or Dubinin-Radushkevich (DR) method for CO_2. The BET surface area (S_{BET}) was calculated in the relative pressure range of 0.05–0.3 for N_2 adsorption. The pore size distribution (PSD) was calculated using a non-local density functional theory (NLDFT) method for slit pores adapted for these materials. Before the gas adsorption analysis samples were degassed overnight under vacuum at 200 °C. Raman spectra were measured using a Renishaw in Via Raman instrument with a laser wavelength of 633 nm. X-ray photoelectron spectroscopy (XPS) was performed using a Thermo Scientific K-Alpha* instrument with a monochromated Al-Kα X-ray source, after drying the samples at 120ºC overnight. Atomic compositions were obtained from averaged spectra took from 3 areas for each sample. Small/wide angle X-ray scattering

(SAXS/WAXS) was measured on a Xenocs nano-InXider with a Cu-kα source and a two-detector setup for combined SAXS/WAXS measurements. Powder samples were packed in 2 mm Kapton capillaries and measured for 10 min, the empty capillary was measured separately and used for background subtraction. Neutron total scattering experiments were performed at the NIMROD[76] instrument at ISIS (Harwell, UK), each sample was contained in a thin-walled Vanadium flat plate cell measured for 2 hours using a 30x30mm beam. The data were normalised using a 3mm VNb null scattering plate and scattering from the empty cell and instrument subtracted. Data were normalised to and absolute scale and corrected for beam attenuation, multiple-scattering and inelasticity effects using the Gudrun programme.[77]

Electrochemical measurements: Electrodes were made using an 85:5:10 weight ratio of active material hard carbon made by hydrothermal carbonisation method, carbon black (Super P conductive, 99+%, Alfa Aesar), and carboxymethyl cellulose binder (CMC) (Mw~250,000, Sigma Aldrich), respectively. The obtained slurry was coated in a 250 µm layer on Al foil (conductive carbon coated, 18 µm, MTI corporation) by doctor blade and dried at room temperature for 24h and then at 100˚C for 2 h under vacuum. The electrolyte and half-cell preparation were conducted in an argon-filled glove box with H_2O < 0.5 ppm, O_2 < 0.5 ppm. The CR2032 coin cells were assembled with a sodium metal disc (1 mm thick, sodium ingot, 99.8% metals basis, Alfa Aesar) as a counter electrode (CE), and a disordered, hard carbon anode as the working electrode (WE). Whatman GF/B glass microfibre was used as a separator. A 1 M electrolyte solution containing predried (80 °C overnight) sodium hexafluorophosphate ($NaPF_6$ Alfa Aesar, 99+%) in predried (in 4 Å porous molecular sieves, overnight) 1:1 volume mixture of ethylene carbonate (EC, anhydrous 99%, Sigma Aldrich) and dimethyl carbonate (DMC, 99.9+%, Sigma Aldrich) was prepared by stirring until fully dissolved. Galvanostatic cycling tests were performed on a Basytec system in the potential range of 0.001-2.5 V *vs* Na^+/Na. Sodiation/desodiation current rate was 30 mA g^{-1}. which corresponds to a cycling rate of C/10. Electrochemical Dilatometry setup (ECD-3-nano cell by EL-CELL GmbH) was employed to study the electrode dynamics during cycling. ECD-nano cells are designed in a way that only quantifies the dilation of the working electrode in one dimension by the help of a sensor during electrochemical cycling. The tests were performed in a three electrode-cell configuration having 10 mm diameter of electrode (here hard carbon) as the working electrode and of sodium metal as the counter (12 mm diameter) and reference electrodes. A special ceramic porous separator, which was soaked by around in 400µL of electrolyte to wet the electrode, was fixed in position between a metal frame and spring. Therefore, only the

dilatation of the electrode was recorded. The cells were cycled galvanostatically at 10 mA g^{-1} at constant temperature (25°C) in a chamber.

Computational Methods: For the atomic scale simulations of Na storage on defective graphene surfaces and in graphitic stacks with different interlayer distances, all calculations were conducted using density functional theory (DFT) as implemented in the Vienna Ab initio Simulation Package (VASP, version 5.3.5).[78–81] To simulate sodium storage and migration in the planar graphitic layers with varying interlayer distance, a 4×4×2 supercell (64 atoms) was constructed, whereby up to eight sodium was added to each cell in between the two planar graphitic layers. The two planar graphitic layers were placed in an AB stacking mode, whilst varying the interlayer distance (d_{002} according to experimental characterisation). For the calculations of sodium on defective graphitic surfaces, we used graphene to simulate the hard carbon basal plane. Based on previous experience of modelling this kind of systems, an 8 × 8 supercell (without defects 72 carbon atoms) with a converged vacuum gap of 15 Å was used.[82] All calculations used the projector-augmented wave method (PAW) to describe the ion-electron interaction.[83] The plane wave cut-off and k-space integrals were chosen so that the total energy was converged to 1 meV/atom. The kinetic energy cut-off was 800 eV, with a 5×5×2 Γ-centred Monkhorst-Pack grid to sample the Brillouin zone for the graphitic systems and a 9×9×1 Γ-centred Monkhorst-Pack grid for the graphene models. [84] To express the interacting electron exchange-correlation energy, the generalized gradient approximation (GGA) with Perdew-Burke-Ernzerhof (PBE) [85,86] functionals were used (with electronic convergence criteria of 10^{-5} eV and ionic convergence criteria of 10^{-3} eV·$Å^{-1}$). All calculations were performed spin-polarized and are periodic. Due to the large polarizability of the graphite and sodium, it is necessary to include dispersion corrections to accurately estimate the metal adsorption and binding energies, in addition to eh graphitic interlayer binding energy. [87–89] Here, the DFT-D3 method with Becke-Johnson damping by Grimme and co-workers was selected. [90,91]

Acknowledgements

The authors would like to thank the Engineering and Physical Sciences Research Council for funding (EP/R021554/1). H.Al would like to acknowledge the funding provided by the Republic of Turkey Ministry of National Education. E.O. would like to acknowledge the use of Athena at HPC Midlands+, which was funded by the EPSRC under grant EP/ P020232/1, and the Eureka HPC cluster at the University of Surrey. We are grateful to the UK Materials

and Molecular Modelling Hub for computational resources, which is partially funded by EPSRC (EP/P020194/1).

Author contributions

H.Al designed the study and drafted the article. H.Al. and H.Au synthesised the hard carbon samples and conducted the electrochemical testing for the NIB cells. H.Al obtained the SEM, gas adsorption experiments and Raman data. H.Au and H.Al. conducted XPS, TEM experiment. A.C.S.J. conducted the SAXS/WAXS measurements and analysis. A.C.S.J. and T.F.H. performed the SANS/WANS measurements and analysis. E.O. performed the DFT simulations and analysis. M.G and H.Al conducted the *in-situ* electrochemical dilatometry experiment. H.Au, E.O., A.C.S.J., an M.G. revised and edited the manuscript. P.A., Q.C., A.J.D. and M.-M.T. provided supervision and funding, and revised and edited the final manuscript.

References

1. Larcher, D. & Tarascon, J.-M. Towards greener and more sustainable batteries for electrical energy storage. *Nat. Chem.* **7**, 19–29 (2015).
2. Lewis, N. S. Powering the Planet. *MRS Bull.* **32**, 808–820 (2007).
3. International Energy Agency Key World Energy Statistics 2011 (IEA, 2011); available at http://www.iea.org/publications/freepublications/publication/ key_world_energy_stats-1.pdf.
4. Grey, C. P. & Tarascon, J. M. Sustainability and in situ monitoring in battery development. *Nat. Publ. Gr.* **16**, (2017).
5. Saurel, D., Orayech, B., Xiao, B., Carriazo, D. & Li, X. From Charge Storage Mechanism to Performance : A Roadmap toward High Specific Energy Sodium-Ion Batteries through Carbon Anode Optimization. **1703268**, 1–33 (2018).
6. Hwang, J.-Y., Myung, S.-T. & Sun, Y.-K. Sodium-ion batteries: present and future. *Chem. Soc. Rev.* **46**, 3529–3614 (2017).
7. Ponrouch, A. *et al.* Non-aqueous electrolytes for sodium-ion batteries. *J. Mater. Chem. A* **3**, 22–42 (2015).
8. Barpanda, P., Oyama, G., Nishimura, S., Chung, S.-C. & Yamada, A. A 3.8-V earth-abundant sodium battery electrode. *Nat. Commun.* **5**, 4358 (2014).
9. Zhou, G. *et al.* Graphene-Wrapped Fe $_3$ O $_4$ Anode Material with Improved Reversible Capacity and Cyclic Stability for Lithium Ion Batteries. *Chem. Mater.* **22**, 5306–5313 (2010).
10. Lu, L., Han, X., Li, J., Hua, J. & Ouyang, M. A review on the key issues for lithium-ion battery management in electric vehicles. *J. Power Sources* **226**, 272–288 (2013).
11. Li, L. *et al.* Recent progress on sodium ion batteries: potential high-performance anodes. *Energy Environ. Sci.* **11**, 2310–2340 (2018).
12. Li, Y., Hu, Y.-S. S., Titirici, M.-M. M., Chen, L. & Huang, X. Hard Carbon Microtubes Made from Renewable Cotton as High-Performance Anode Material for Sodium-Ion Batteries. *Adv. Energy Mater.* **6**, 1600659 (2016).
13. Ge, P. & Fouletier, M. Electrochemical intercalation of sodium in graphite. *Solid State Ionics* **28**–**30**, 1172–1175 (1988).
14. Metrot, A., Guerard, D., Billaud, D. & Herold, A. New results about the sodium-graphite system. *Synth. Met.* **1**, 363–369 (1980).
15. Luo, W. *et al.* Na-Ion Battery Anodes: Materials and Electrochemistry. *Acc. Chem. Res.* **49**, 231–240 (2016).
16. Recent advances of electrode materials for low-cost sodium-ion batteries towards practical application for grid energy storage. *Elsevier*
17. Stevens, D. A. & Dahn, J. R. High Capacity Anode Materials for Rechargeable Sodium-Ion Batteries. *J. Electrochem. Soc.* **147**, 1271 (2000).
18. Komaba, S. *et al.* Electrochemical Na Insertion and Solid Electrolyte Interphase for Hard-Carbon Electrodes and Application to Na-Ion Batteries. *Adv. Funct. Mater.* **21**, 3859–3867 (2011).
19. Irisarri, E., Ponrouch, A. & Palacin, M. R. Review—Hard Carbon Negative Electrode Materials for Sodium-Ion Batteries. *J. Electrochem. Soc.* **162**, A2476–A2482 (2015).
20. Li, Y. *et al.* Pitch-derived amorphous carbon as high performance anode for sodium-ion batteries. *Energy Storage Mater.* **2**, 139–145 (2016).
21. Hou, H., Qiu, X., Wei, W., Zhang, Y. & Ji, X. Carbon Anode Materials for Advanced Sodium-Ion Batteries. *Adv. Energy Mater.* **7**, 1602898 (2017).
22. Li, Y. *et al.* Advanced sodium-ion batteries using superior low cost pyrolyzed anthracite anode: towards practical applications. *Energy Storage Mater.* **5**, 191–197 (2016).
23. Bommier, C. & Ji, X. Recent Development on Anodes for Na-Ion Batteries. *Isr. J. Chem.* **55**, 486–507 (2015).
24. Balogun, M.-S., Luo, Y., Qiu, W., Liu, P. & Tong, Y. A review of carbon materials and their composites with alloy metals for sodium ion battery anodes. *Carbon N. Y.* **98**, 162–178 (2016).
25. Alcántara, R., Lavela, P., Ortiz, G. F. & Tirado, J. L. Carbon Microspheres Obtained from Resorcinol-Formaldehyde as High-Capacity Electrodes for Sodium-Ion Batteries.

Electrochem. Solid-State Lett. **8**, A222 (2005).
26. Bommier, C., Mitlin, D. & Ji, X. Internal structure – Na storage mechanisms – Electrochemical performance relations in carbons. *Prog. Mater. Sci.* **97**, 170–203 (2018).
27. Thomas, P. & Billaud, D. Sodium electrochemical insertion mechanisms in various carbon fibres. *Electrochim. Acta* **46**, 3359–3366 (2001).
28. Stevens, D. A. & Dahn, J. R. The Mechanisms of Lithium and Sodium Insertion in Carbon Materials. *J. Electrochem. Soc.* **148**, A803 (2001).
29. Cao, Y. *et al.* Sodium ion insertion in hollow carbon nanowires for battery applications. *Nano Lett.* **12**, 3783–3787 (2012).
30. Tang, K. *et al.* Hollow carbon nanospheres with superior rate capability for sodium-based batteries. *Adv. Energy Mater.* **2**, 873–877 (2012).
31. Bommier, C. *et al.* Predicting capacity of hard carbon anodes in sodium-ion batteries using porosity measurements. *Elsevier*
32. Luo, W. *et al.* Low-Surface-Area Hard Carbon Anode for Na-Ion Batteries via Graphene Oxide as a Dehydration Agent. *ACS Appl. Mater. Interfaces* **7**, 39 (2015).
33. Xiao, L. *et al.* Hard carbon nanoparticles as high-capacity, high-stability anodic materials for Na-ion batteries. *Nano Energy* **19**, 279–288 (2016).
34. Luo, W. *et al.* Carbon nanofibers derived from cellulose nanofibers as a long-life anode material for rechargeable sodium-ion batteries. *J. Mater. Chem. A* **1**, 10662–10666 (2013).
35. Hou, H., Qiu, X., Wei, W., Zhang, Y. & Ji, X. Carbon Anode Materials for Advanced Sodium-Ion Batteries. *Advanced Energy Materials* **7**, (2017).
36. Qiu, S. *et al.* Manipulating Adsorption–Insertion Mechanisms in Nanostructured Carbon Materials for High-Efficiency Sodium Ion Storage. *Adv. Energy Mater.* **7**, (2017).
37. Sun, N., Liu, H. & Xu, B. Facile synthesis of high performance hard carbon anode materials for sodium ion batteries. *J. Name* **00**, 1–3 (2013).
38. Morcrette, M., Chabre, Y., Vaughan, G., … G. A.-E. & 2002, undefined. In situ X-ray diffraction techniques as a powerful tool to study battery electrode materials. *Elsevier*
39. Placke, T. *et al.* In situ X-ray Diffraction Studies of Cation and Anion Inter-calation into Graphitic Carbons for Electrochemical Energy Storage Applications. *Zeitschrift für Anorg. und Allg. Chemie* **640**, 1996–2006 (2014).
40. Whitehead, A., Edström, K., Rao, N., sources, J. O.-J. of power & 1996, undefined. In situ X-ray diffraction studies of a graphite-based Li-ion battery negative electrode. *Elsevier*
41. Han, M. *et al.* In situ atomic force microscopy study of nano-micro sodium deposition in ester-based electrolytes. *Chem. Commun.* **54**, 2381–2384 (2018).
42. Jeong, S. *et al.* AFM study of surface film formation on a composite graphite electrode in lithium-ion batteries. *Elsevier*
43. Lacey, S. D. *et al.* Atomic force microscopy studies on molybdenum disulfide flakes as sodium-ion anodes. *Nano Lett.* **15**, 1018–1024 (2015).
44. Goktas, M. *et al.* Graphite as Cointercalation Electrode for Sodium-Ion Batteries: Electrode Dynamics and the Missing Solid Electrolyte Interphase (SEI). *Adv. Energy Mater.* **8**, 1702724 (2018).
45. Klein, F., Pinedo, R., Berkes, B. B., Janek, J. & Adelhelm, P. Kinetics and Degradation Processes of CuO as Conversion Electrode for Sodium-Ion Batteries: An Electrochemical Study Combined with Pressure Monitoring and DEMS. *J. Phys. Chem. C* **121**, 8679–8691 (2017).
46. Huesker, J. *et al.* In situ dilatometric study of the binder influence on the electrochemical intercalation of bis (trifluoromethanesulfonyl) imide anions into graphite. *Elsevier*
47. Winter, M., Wrodnigg, G. H., Besenhard, J. O., Biberacher, W. & Novák, P. *Dilatometric Investigations of Graphite Electrodes in Nonaqueous Lithium Battery Electrolytes*. (2000).
48. Gómez-Cámer, J., Bünzli, C., Hantel, M., Carbon, T. P.- & 2016, undefined. On the correlation between electrode expansion and cycling stability of graphite/Si electrodes for Li-ion batteries. *Elsevier*
49. Armand, M. & Touzain, P. Graphite intercalation compounds as cathode materials. *Mater. Sci. Eng.* **31**, 319–329 (1977).

50. Qiu, S. *et al.* Manipulating Adsorption-Insertion Mechanisms in Nanostructured Carbon Materials for High-Efficiency Sodium Ion Storage. *Adv. Energy Mater.* **7**, 1700403 (2017).
51. Komaba, S. *et al.* Electrochemical Na Insertion and Solid Electrolyte Interphase for Hard-Carbon Electrodes and Application to Na-Ion Batteries. *Adv. Funct. Mater.* **21**, 3859–3867 (2011).
52. Dahbi, M., Yabuuchi, N., Kubota, K., Tokiwa, K. & Komaba, S. Negative electrodes for Na-ion batteries. *Phys. Chem. Chem. Phys.* **16**, 15007 (2014).
53. Stevens, D. A. & Dahn, J. R. High capacity anode materials for rechargeable sodium-ion batteries. *J. Electrochem. Soc.* **147**, 1271–1273 (2000).
54. Komaba, S. *et al.* Electrochemical Na insertion and solid electrolyte interphase for hard-carbon electrodes and application to Na-ion batteries. *Adv. Funct. Mater.* **21**, 3859–3867 (2011).
55. Titirici, M.-M., White, R. J., Falco, C. & Sevilla, M. Black perspectives for a green future: hydrothermal carbons for environment protection and energy storage. *Energy Environ. Sci.* **5**, 6796 (2012).
56. Stevens, D. A. & Dahn, J. R. An In Situ Small-Angle X-Ray Scattering Study of Sodium Insertion into a Nanoporous Carbon Anode Material within an Operating Electrochemical Cell. *J. Electrochem. Soc.* **147**, 4428 (2000).
57. Cychosz, K. A., Guillet-Nicolas, R., García-Martínez, J. & Thommes, M. Recent advances in the textural characterization of hierarchically structured nanoporous materials. *Chem. Soc. Rev.* **46**, 389–414 (2017).
58. Ferrari, A. C. & Basko, D. M. Raman spectroscopy as a versatile tool for studying the properties of graphene. *Nat. Nanotechnol.* **8**, 235–246 (2013).
59. Ferrari, A. C. & Robertson, J. Interpretation of Raman spectra of disordered and amorphous carbon. *Phys. Rev. B* **61**, 14095–14107 (2000).
60. Ferrari, A. C. *et al.* Raman Spectrum of Graphene and Graphene Layers. (2006). doi:10.1103/PhysRevLett.97.187401
61. Casiraghi, C., Ferrari, A. C. & Robertson, J. Raman spectroscopy of hydrogenated amorphous carbons. *Phys. Rev. B* **72**, 085401 (2005).
62. Titirici, M.-M., Antonietti, M. & Baccile, N. Hydrothermal carbon from biomass: a comparison of the local structure from poly- to monosaccharides and pentoses/hexoses. *Green Chem.* **10**, 1204 (2008).
63. Augustyn, V., Simon, P. & Dunn, B. Pseudocapacitive oxide materials for high-rate electrochemical energy storage. *Energy and Environmental Science* **7**, 1597–1614 (2014).
64. Wang, J., Polleux, J., Lim, J. & Dunn, B. Pseudocapacitive contributions to electrochemical energy storage in TiO 2 (anatase) nanoparticles. *J. Phys. Chem. C* **111**, 14925–14931 (2007).
65. Matei Ghimbeu, C. *et al.* Insights on the Na+ ion storage mechanism in hard carbon: Discrimination between the porosity, surface functional groups and defects. *Nano Energy* **44**, 327–335 (2018).
66. Zhang, B., Ghimbeu, C. M., Laberty, C., Vix-Guterl, C. & Tarascon, J.-M. Correlation Between Microstructure and Na Storage Behavior in Hard Carbon. *Adv. Energy Mater.* **6**, 1501588 (2016).
67. Bommier, C., Surta, T. W., Dolgos, M. & Ji, X. New Mechanistic Insights on Na-Ion Storage in Nongraphitizable Carbon. *Nano Lett.* **15**, 5888–5892 (2015).
68. Goktas, M. *et al.* Graphite as Cointercalation Electrode for Sodium-Ion Batteries: Electrode Dynamics and the Missing Solid Electrolyte Interphase (SEI). *Adv. Energy Mater.* **8**, (2018).
69. Tsai, P., Chung, S.-C., Lin, S. & Yamada, A. Ab initio study of sodium intercalation into disordered carbon. *J. Mater. Chem. A* **3**, 9763–9768 (2015).
70. Nakada, K. & Ishii, A. Migration of adatom adsorption on graphene using DFT calculation. *Solid State Commun.* **151**, 13–16 (2011).
71. Xu, Z. *et al.* Dispersion-corrected DFT investigation on defect chemistry and potassium migration in potassium-graphite intercalation compounds for potassium ion batteries anode materials. *Carbon N. Y.* **107**, 885–894 (2016).
72. Olsson, E., Chai, G., Dove, M. & Cai, Q. Adsorption and migration of alkali metals (Li, Na, and K) on pristine and defective graphene surfaces. *Nanoscale* **11**, 5274–5284 (2019).

73. Raebiger, H., Lany, S. & Zunger, A. Origins of the p-type nature and cation deficiency in Cu2 O and related materials. *Phys. Rev. B* **76**, 045209 (2007).
74. Oba, F., Choi, M., Togo, A. & Tanaka, I. Point defects in ZnO: an approach from first principles. *Sci. Technol. Adv. Mater.* **12**, 034302 (2011).
75. Zhang, S. & Northrup, J. Chemical potential dependence of defect formation energies in GaAs: Application to Ga self-diffusion. *Phys. Rev. Lett.* **67**, 2339–2342 (1991).
76. Professor Martin Dove et al; (2018). Local structure study of non-graphitisable carbon anode for sodium batteries. *STFC ISIS Neutron Muon Source* doi:10.5286/ISIS.E.RB1810728
77. Soper, A. K. Rutherford Appleton Laboratory Technical Report RAL-TR-2011-013. (2011).
78. Kresse, G. & Furthmüller, J. Efficiency of ab-initio total energy calculations for metals and semiconductors using a plane-wave basis set. *Comput. Mater. Sci.* **6**, 15–50 (1996).
79. Kresse, G. & Furthmüller, J. Efficient iterative schemes for ab initio total-energy calculations using a plane-wave basis set. *Phys. Rev. B. Condens. Matter* **54**, 11169–11186 (1996).
80. Kresse, G. & Hafner, J. Ab initio molecular-dynamics simulation of the liquid-metal–amorphous-semiconductor transition in germanium. *Phys. Rev. B* **49**, 14251 (1994).
81. Kresse, G. & Hafner, J. Ab initio molecular dynamics for liquid metals. *Phys. Rev. B* **47**, 558 (1993).
82. Olsson, E., Chai, G., Dove, M. & Cai, Q. Adsorption and migration of alkali metals (Li, Na, and K) on pristine and defective graphene surfaces. *Nanoscale* **11**, 5274–5284 (2019).
83. Blöchl, P. E. Projector augmented-wave method. *Phys. Rev. B* **50**, 17953 (1994).
84. Monkhorst, H. J. & Pack, J. D. Special points for Brillouin-zone integrations. *Phys. Rev. B* **13**, 5188–5192 (1976).
85. Perdew, J., Burke, K. & Ernzerhof, M. Errata: Generalized Gradient Approximation Made Simple. *Phys. Rev. Lett.* **77**, 1396 (1997).
86. Perdew, J., Burke, K. & Ernzerhof, M. Generalized Gradient Approximation Made Simple. *Phys. Rev. Lett.* **77**, 3865–3868 (1996).
87. Fan, X., Zheng, W. T., Kuo, J.-L. L. & Singh, D. J. Adsorption of single Li and the formation of small Li clusters on graphene for the anode of lithium-ion batteries. *ACS Appl. Mater. Interfaces* **5**, 7793–7797 (2013).
88. Amft, M., Lebègue, S., Eriksson, O. & Skorodumova, N. V. Adsorption of Cu, Ag, and Au atoms on graphene including van der Waals interactions. *J. Phys. Condens. Matter* **23**, 395001 (2011).
89. Lee, S., Lee, M., Choi, H., Yoo, D. S. & Chung, Y. C. Effect of nitrogen induced defects in Li dispersed graphene on hydrogen storage. *Int. J. Hydrogen Energy* **38**, 4611–4617 (2013).
90. Becke, A. D. & Johnson, E. R. Density-functional thermochemistry. III. The role of exact exchange. *J. Chem. Phys.* **123**, 154108 (2005).
91. Grimme, S., Ehrlich, S. & Goerigk, L. Effect of the Damping Function in Dispersion Corrected Density Functional Theory. *J. Comput. Chem.* **32**, 1456 (2011).